[4] S. Zhao and G. Wang, "Feldkamp-type cone-beam tomography in the wavelet framework," *IEEE Trans. Med. Imag.*, vol. 19, pp. 922–929, Sept. 2000.
[5] A. V. Bronnikov, "A filtering approach to image reconstruction in 3D SPECT," *Phys. Med. Biolog.*, vol. 45, pp. 2639–2651, 2000.
[6] D. L. Donoho and I. M. Johnstone, "Ideal spatial adaptation by wavelet shrinkage," *Ann. Statist.*, vol. 81, pp. 425–455, 1994.
[7] A. Rosenfeld and A. C. Kak, *Digital Picture Processing I.* New York: Academic, 1982.
[8] I. Daubechies, *Ten Lectures on Wavelets*. Philadelphia, PA: SIAM, 1992.
[9] L. Cavalier and J.-Y. Koo, "Poisson intensity estimation for tomographic data using a wavelet shrinkage approach,", manuscript.
[10] F. Anscombe, "The transformation of Poisson, binomial and negative binomial data," *Biometrika*, vol. 35, pp. 246–254, 1948.
[11] J. R. Lee, Y. Choi, Y. S. Choe, K. H. Lee, S. E. Kim, S. A. Shin, and B.-T. Kim, "Performance measurements of positron emission tomography: An investigation using general electric advanceTM," *Korean J. Nucl. Med.*, vol. 30, pp. 548–559, 1996.
[12] T. R. DeGrado, T. G. Turkington, J. J. Williams, C. W. Stearns, J. M. Hoffman, and R. E. Coleman, "Performance characteristics of a whole-body PET scanner," *J. Nucl. Med.*, vol. 35, pp. 1398–1406, 1994.
[13] N.-Y. Lee, "Wavelet Vaguelette Decompositions and Homogeneous Equations," Ph.D. dissertation, Purdue Univ., West Lafayette, IN, 1997.
[14] F. E. Turkheimer, M. Brett, D. Visvikis, and V. J. Cunningham, "Multiresolution analysis of emission tomography images in the wavelet domain," *J. Cereb. Blood Flow Metab.*, vol. 19, pp. 1189–1208.
[15] R. Coifman and D. L. Donoho, "Translation invariant de-noising," in *Lecture Notes in Statistics*, A. Antoniadis and G. Oppenheim, Eds. Berlin, Germany: Springer-Verlag, 1995, Wavelet and Statistics, pp. 125–150.

Fast and Robust Optic Disc Detection Using Pyramidal Decomposition and Hausdorff-Based Template Matching

Marc Lalonde, Mario Beaulieu, and Langis Gagnon*

***Abstract*—We report about the design and test of an image processing algorithm for the localization of the optic disk (OD) in low-resolution (about 20 μ/pixel) color fundus images. The design relies on the combination of two procedures: 1) a Hausdorff-based template matching technique on edge map, guided by 2) a pyramidal decomposition for large scale object tracking. The two approaches are tested against a database of 40 images of various visual quality and retinal pigmentation, as well as of normal and small pupils. An average error of 7% on OD center positioning is reached with no false detection. In addition, a confidence level is associated to the final detection that indicates the "level of difficulty" the detector has to identify the OD position and shape.**

***Index Terms*—Ophthalmic imaging, image analysis, image segmentation, template matching.**

I. Introduction

The aim of this paper is to present the performance of a simple, though fast and robust detection tool for the localization and segmentation of the optic disk (OD) in low-resolution color fundus images. Segmenting the OD is a key pre-processing element in many algorithms designed for "automatic" anatomical structures extraction and retinal lesions detection, notably for

- vessel tree extraction, for which large vessels located in the vicinity of the OD serve as seeds for vessel tracking [1]–[3];
- macula (fovea) detection, where the constant distance between the OD and the macula center is used as *a priori* knowledge to help positionning the macula [4];
- retinopathy-related lesions detection, to help improve the detection rate by masking the OD [5].

Curiously, not much literature exists on the problem of detecting the OD without user intervention. Tolias and Panas use linguistic descriptions to automatically specify the OD location, based on the hypothesis that the OD is a bright region located either in the left-center or right-center of the fundus image [1]. This assumption is not always true in practice and certainly not for our image database. Kochner *et al.* use Hough transform and steerable filters to automatically detect the location and size of the OD [2]. Points belonging to the edges of the main vessel branches are extracted using steerable filters (first-order Gaussian filter kernels at varying orientations) and fitted to an ellipse via a Hough transform. From this, an approximate location of the OD is obtained on one end of the ellipse major axis. The location and size are then refined using a hierarchical filtering scheme based on first-order steerable filters. Although the approach is appealing, we have not retained it because of 1) the prerequisite of detecting points belonging to the main vessel branches which imposes an additionnal pre-processing step; 2) the computer intensive Hough transform and more importantly; 3) the necessity to have image centered on the macula in order to see the elliptical shape of the two main branches of the vessel tree.

Our approach attempts to respond to three user-specific and computational specifications:

1) robustness to the variable appearance of ODs (intensity, color, contour definition, macula-centered and OD-centered images);
2) detection performance above 90%;
3) short computation time.

Furthermore, the technique being sought does not need to provide a precise identification of the OD contour because the result will not be used for diagnosis purposes like e.g., contour feature extraction for glaucoma grading. However, the method must be fast and robust enough because other tools we are developing are dependent upon its performance, namely macula detection and vessel extraction.

To reach this goal, we found that the combination of the following independent image processing tools yielded satisfactory results: 1) template-based matching technique on edge map using a Hausdorff distance measure, guided by 2) scale tracking of large objects using multiresolution image decomposition. Tools cooperation is achieved through combination of confidence indexes associated with various detected OD candidates.

The paper is organized as follows. Section II presents a description of the two algorithms used as well as the way they are combined. Section III provides a detailed report of performance measures resulting from a test on a database of 40 images including images 1) of low visual quality; 2) macula-centered and OD-centered; 3) of various retinal pigmentation as well as 4) of normal and small pupils. Conclusion, comments and possible further works are mentioned in Section IV.

II. Algorithm Description

The algorithm design relies on three assumptions. The first pertains to the image acquisition. Since acquisition of ophthalmic images usually follows a fixed protocol, some information about the retina and its

Manuscript received December 20, 2000; revised August 10, 2001. The Associate Editor responsible for coordinating the review of this paper and recommending its publication was M. W. Vannier. *Asterisk indicates corresponding author.*

M. Lalonde and M. Beaulieu are with the Centre de recherche informatique de Montréal, Montréal, QC H3A 1B9, Canada.

*L. Gagnon is with the Centre de recherche informatique de Montréal, 550 Sherbrooke West, Suite 100, Montréal, QC H3A 1B9, Canada (e-mail: lgagnon@crim.ca).

Publisher Item Identifier S 0278-0062(01)10004-2.

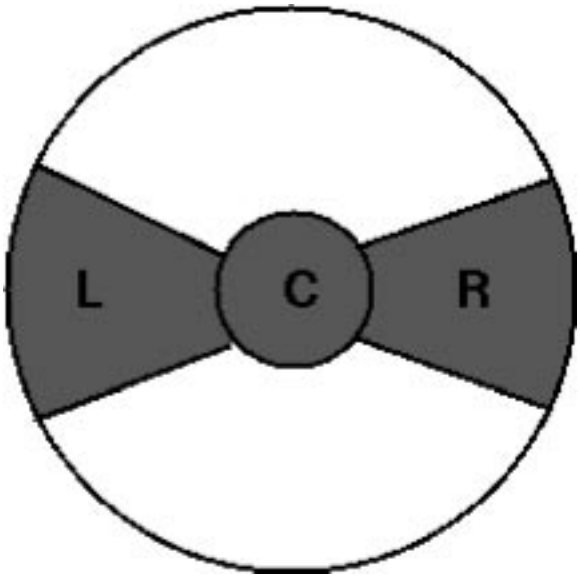

Fig. 1. Restricted search space corresponding to the *a priori* knowledge of the OD position for OD-centered images (C), macula-centered left eye (L), and macula-centered right eye (R).

structures can be deduced and exploited. The practitioner knows which eye (left/right) is being imaged and whether the image is centered on the macula or the optic disc (OD). This *a priori* information should be exploited in order to guide the search for the OD in a specific portion of the image (Fig. 1). The second assumption comes from observations that the OD represents a bright region (not necessarily the brightest) in an ophthalmic image of good quality. The last assumption relates to the form of the OD, which always appears approximately circular.

The method we propose is decomposed into two stages.

- OD tracking through a pyramidal decomposition.
- OD contour search technique based on the Hausdorff distance.

Each stage generates a set of hypotheses. These hypotheses are analyzed and combined to provide the best solution.

A. Locating Potential OD Areas Using a Pyramidal Decomposition

Potential regions which might contain the optic disc are first found by means of a pyramidal decomposition on the grayscale representation of the input color image (hue variability across subjects, particularly those of different ethnic backgrounds, seems to reduce the usefulness of color cues in ophthalmic image analysis). For simplicity, the green channel (G) of the original RGB image has been selected as the grayscale representation, but other representations (e.g., the intensity channel of the corresponding HSI image) could be used with similar results. For implementation efficiency, the pyramid is created using a simple Haar-based discrete wavelet transform for which the high-pass and low-pass filters are $[1, -1]$ and $[1, 1]$ respectively [6].

Fig. 3 gives an example of a four- and five-level decomposition on an image of our data set. As one can see, these resolution levels are commensurate with the OD dimension as only a few bright pixels fall into the original OD region.

Because of the small image size at the lowest resolution and the vanishing of small bright regions (which happen to be lesions such as exudates) over the pyramid, the search for the OD region becomes a rapid operation with few false candidates. This is further facilitated by restricting the search to the portion of the original image according to the *a priori* knowledge about the OD position as mentioned in Section II.

Pixels in the low-resolution image which have the highest intensity values compared with the mean pixel intensity over the search area yield possible region candidates in the original image. Within each of these regions, smoothing is performed and the brightest pixel is selected as a possible OD center point. A simple confidence value denoted by CV_R may be computed to assess the relevance of each hypothesis. CV_R is defined as the ratio between the average pixel intensity inside a circular region of fixed radius centered on the brightest pixel and the average intensity in its neighborhood. The measurement is designed to "capture" one expected property of optic discs, namely a roughly circular patch of bright pixels surrounded by darker pixels. Note that the radius of the circular region is chosen to be approximately equal to the expected radius of the optic disc in the image (the physical diameter of the optic disc is about 1.5 mm on average). The neighborhood is simply a rectangle slightly larger than the bounding box around the circular region.

At this point, the intermediate result is a list of high-intensity pixel coordinates representing the center of potential OD regions, along with their confidence values CV_R. The top ten candidates are retained for further analysis.

B. Locating Potential OD Contours Using Hausdorff Distance

The search for the OD contour is performed using an algorithm based on the Hausdorff distance and initially implemented for symbol recognition in utility maps [7]. The key idea is that the areas identified by the pyramidal decomposition method are explored for the presence of a circular shape, as if the OD was a symbol in a map. The process goes as the following.

1) Aggregate pyramidal candidate regions.
2) For each aggregated region:
   a) perform edge detection and do thresholding;
   b) perform Hausdorff-based matching;
   c) eliminate redundant solutions.
3) Compute confidence level for each solution.

1) Region of Interest (ROI) Aggregation: In order to limit the number of ROIs, contiguous regions are aggregated into a single zone. Typically, for a retinal image of good quality, one or two search zones may result from this aggregation.

2) Edge Detection: Edge detection is performed on the green band of the original color image in each of the search zones. Since Hausdorff-based matching requires binary images as inputs, the magnitude edge image is thresholded following an approach based upon a Rayleigh probabilistic modeling of the noisy edge distribution [8], [9]. Within this framework, selecting the threshold requires choosing a probability of misinterpreting a noisy edge as a true edge, which implies finding a tradeoff between the risk of discarding valid edges and the risk of retaining too many noisy edges. The former situation prevents the Hausdorff matcher from spotting the OD while the latter increases computation time considerably (see below for an explanation) and raises the probability of false matches. A similar issue is at the core of Rayleigh-based constant false alarm rate (CFAR) detectors in radar imagery [10].

According to Ravid *et al.*, the Rayleigh-based CFAR threshold T can be estimated according to

$$T(x) = \left[\left(P_{\mathrm{FA}}^{-\frac{1}{M}} - 1 \right) \sum_{j=1}^{M} x_j^2 \right]^{\frac{1}{2}} \tag{1}$$

where the x_j's are the magnitudes of M noisy edge samples used for the estimation and P_{FA} is the probability of false alarms (i.e., the probability that a noisy edge is viewed as a valid edge). Of course, since edge maps contain both valid and noisy edges, a strategy must be sought in order to estimate T using the noisy edges only. The procedure we use goes as follows:

1) perform Canny edge detection in the region of interest with the low (L) and high (H) Canny hysterisis thresholds set to capture as many edges as possible (e.g., $L = 1$ and $H = 2$);

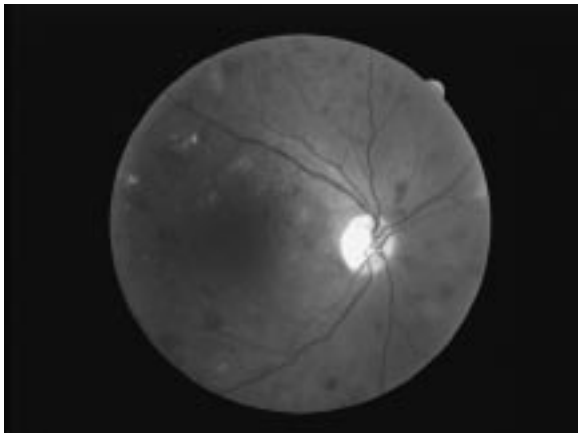

(a)

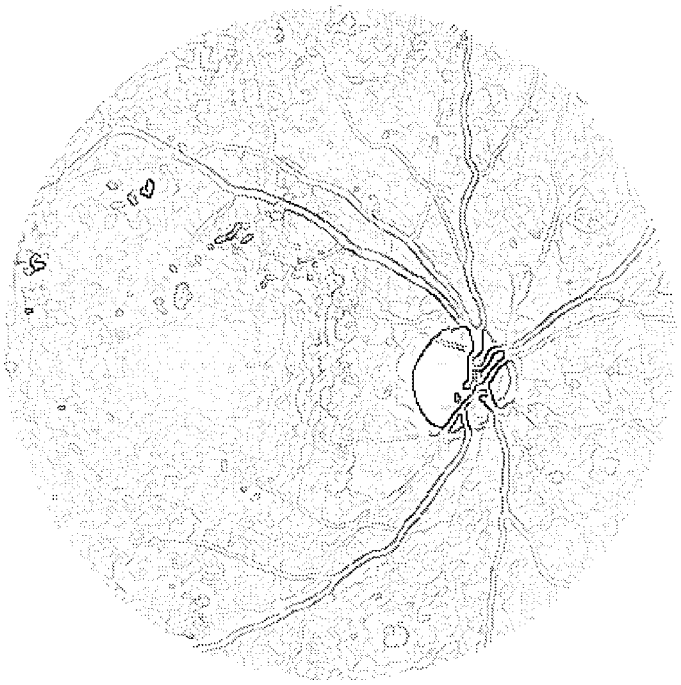

(b)

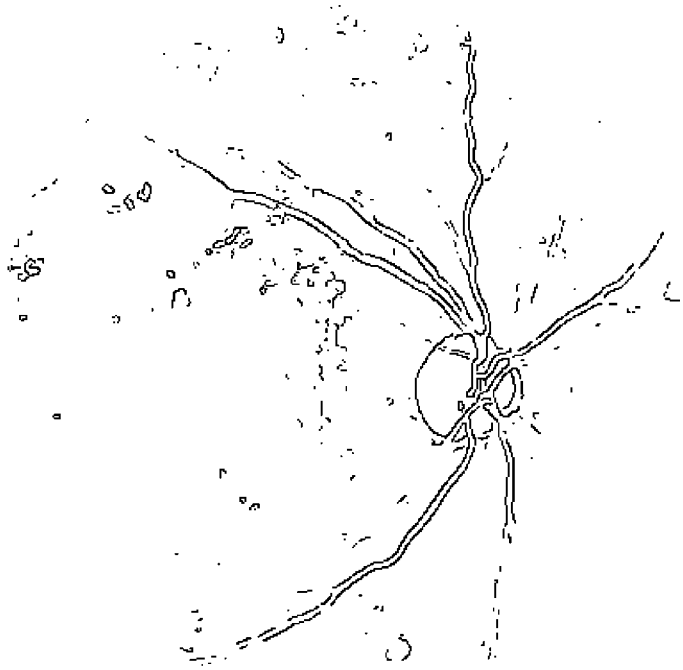

(c)

Fig. 2. Example of edge map thresholding result. (a) Original grey level image (511_2).(b) Edges obtained with low Canny thresholds. (c) Thresholded edge map.

2) reassign the high threshold H to a value that captures 10% of all edges found in Step 1 (with $L = H/2$ as usual) and perform a Canny edge detection again, thus getting an edge map that contains strong edges only;
3) subtract the second edge map from the first to get an approximation of the noisy edge map I_N;
4) extract M edge pixels within a small window in the center of I_N to compute T for a given P_{FA},
5) get the thresholded image I_T using T as the threshold.

The strategy of removing the strongest edges for the estimation of the threshold relies on the assumption that these edges are likely associated to the borders of anatomical structures. As an example, Fig. 2 shows the result of processing a retinal image of fairly good quality. The final binary edge map is used for the Hausdorff-based template matching.

3) Matching With Hausdorff Distance: The Hausdorff distance $H(A, B)$, defined as

$$H(A, B) = \max(h(A, B), h(B, A)) \tag{2}$$

$$h(A, B) = \max_{a \in A} \min_{b \in B} \|a - b\| \tag{3}$$

provides a degree of mismatch between two sets of points A and B by measuring the distance of the point of A that is farthest from any point of B and vice versa [11]. In the current context, A represents the set of black pixels in the binary image I_T (with white background) and B the set of pixels in a white image that form a black circular template (diameter ≈ 60 pixels for a 640×480 image). Locating the OD amounts to evaluating the Hausdorff distance between the template and the underlying arrangement of pixels in I_T; a perfect match yields a zero distance which increases as the resemblance weakens. One remarkable property of Hausdorff-based template matching is its robustness and good performance in locating objects in images of cluttered scenes. This capability is certainly valuable for OD localization given the frequent lack of precise disc borders and the presence of vessels coming out of the disc.

In theory, the Hausdorff distance should be computed at each pixel in I_T but in practice, many optimizations help reduce the processing time substantially [11], [7]. One of them is the use of a Voronoi surface (distance transform). Not only does it allow a fast evaluation of the Hausdorff distance at each location, but it also facilitates the implementation of pruning techniques that eliminate areas of the search

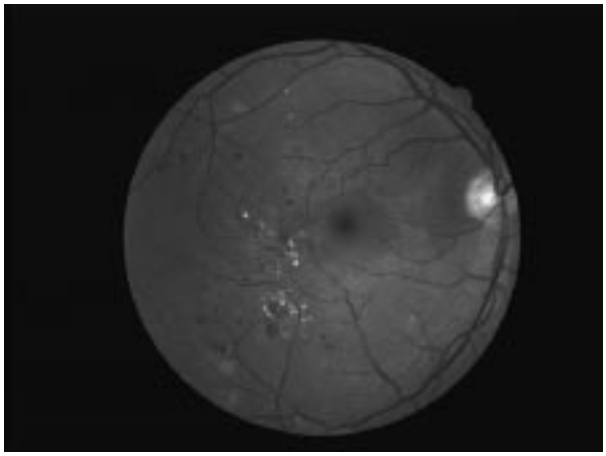

(a)

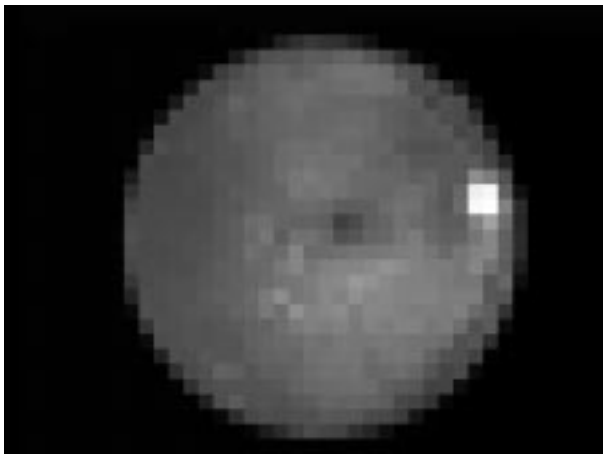

(b)

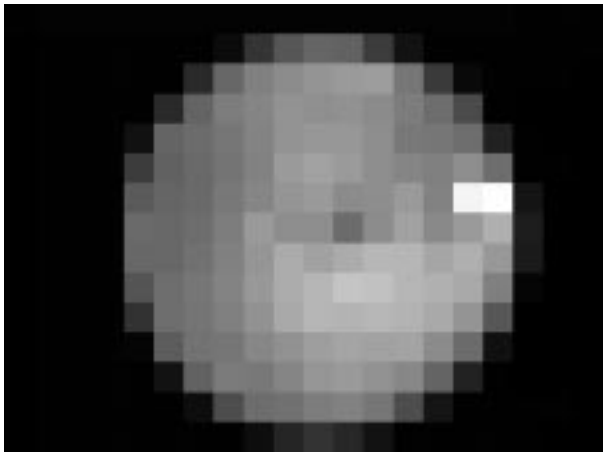

(c)

Fig. 3. Example of pyramidal low frequency subbands. (a) Portion (512×512) of the original grey level image (478_2). (b) Image at the fourth level. (c) Image at the fifth level. At this level, the OD is represented by very few bright pixels.

space around points where the distance is much higher than a given threshold. Pruning is particularly efficient when the input image contains few sparse clusters of black pixels, which is the case when the edge intensity threshold is set appropriately in the previous edge map binarization stage.

In order to account for ODs of varying size, several templates are actually used with a diameter ranging from 54 to 72 pixels. When the Hausdorff distance between a template and I_T is found to be lower than a specified threshold (typically three), a percentage of match is computed and if this rate is reasonable (i.e., a certain proportion of the pixels template are found to overlap edge pixels in I_T, at this location), then the location is retained as the center point of a potential OD candidate. The minimum proportion threshold is set low so as to prevent missing the OD in situations where edge detection and the subsequent thresholding failed to recover the complete contour.

Two confidence values are assigned to each Hausdorff candidates. The first, denoted by CV_H, is the proportion of template pixels overlapping edge pixels in the thresholded edge map I_T. The second, denoted by CV_R, is defined in a similar fashion to that of the pyramidal decomposition candidates, i.e., the ratio between the average pixel intensity over the template candidate and the average intensity over its neighborhood. Again, this indicator is a measure of how well the candidate is aligned with the OD from a pixel-intensity point of view: better aligned candidates having higher CV_R.

C. Determining the Best Candidate

The most likely OD position and radius are found by determining the candidate with the highest overall (global) confidence. The calculation of the global confidence is chosen to follow the rule combination of the Dempster–Shafer theory of evidence which provides a human-like framework to represent, combine and establish a general level of certainty in decision systems, from incomplete or imperfect knowledge [12]. Following Dempster–Shafer theory, the global confidence value CV_G is calculated as

$$\mathrm{CV}_G = \mathrm{CV}_H \times \mathrm{CV}_R + \mathrm{CV}_H \times (1 - \mathrm{CV}_R) + \mathrm{CV}_R \times (1 - \mathrm{CV}_H) \quad (4)$$

Note that the coarse solutions generated at the pyramid decomposition stage obviously get a low global confidence index since the only contributor is the CV_R indicator. In some situations, however, CV_R is high enough to top bad Hausdorff candidates.

III. Results

A. Data Set

A collection of 40 low-resolution fundus images (of about 20 μ/pixel) from 27 persons were acquired using a nonmydriatic Canon color camera CR6-45NM (Table I). An apparent image quality (IQ) index has been evaluated to help interpret the final detection results. Of these 40 images, 16 can be qualified as being of good visual quality ($\mathrm{IQ} = G$), 16 as fair ($\mathrm{IQ} = F$) and eight as bad ($\mathrm{IQ} = B$). Color images of bad quality are those that are blurred and/or have abnormal dark or bright regions. Of course, bad quality images could be discarded by the physician during a diagnosis process but we wanted to keep them in our dataset in order to assess the robustness of the algorithm. Often, regardless of the overall image quality, OD appearance may also be good or bad with respect to the sharpness of its contour and its brightness. These assessments are referred to as OD contour quality (ODCQ) and OD brightness quality (ODBQ) in Table I.

B. Detection Performance

Performance evaluation was made possible by the creation of ground truth (or gold standard) with the help of a paint program (i.e., by manually tracing the OD contour) and by the compilation of performance "measures" such as:

- a matching score S equal to the common area between the true OD region T and the detected one D, and defined as

$$S = \frac{\mathrm{Area}(T \cap D)}{\mathrm{Area}(T \cup D)} \quad (5)$$

TABLE I

PERFORMANCE MEASURES OF THE PROPOSED METHOD WITH RESPECT TO GROUND TRUTH (SEE TEXT FOR DETAILS). COLUMN 1: IMAGE LABEL. COLUMNS 2 AND 3: OD CONTOUR AND BRIGHTNESS QUALITY (ODCQ AND ODBQ, RESPECTIVELY; G STANDS FOR GOOD, F FOR FAIR AND B FOR BAD. COLUMNS 4 TO 6: CONFIDENCE LEVELS C_R AND C_H OF THE TWO BEST PARTICIPANTS IN THE GLOBAL RESULT. COLUMNS 7: MATCHING SCORES S FOR $P_{\mathrm{FA}} = 0.1$. COLUMN 8: ERROR Δ IN THE OD DETECTED CENTER POSITION. COLUMN 9: APPARENT OD DETECTION QUALITY (ODDQ)

Image	IQ	ODCQ	ODBQ	$C_R(\%)$	$C_H(\%)$	$C_G(\%)$	$S(\%)$	Δ(pixels)	ODDQ
278_1	G	F	G	90	50	**95**	91	0.0	**G**
476_1	F	F	F	51	0	**51**	73	5.0	**G**
478_2	G	F	G	90	0	**90**	71	8.1	**G**
478_3	G	G	G	90	29	**93**	84	3.6	**G**
478_4	F	G	G	55	29	**68**	85	4.1	**G**
479_2	G	G	G	90	31	**93**	87	3.0	**G**
501_1	B	B	B	4	30	**33**	94	2.2	**G**
501_4	B	B	F	14	12	**24**	77	5.4	**G**
502_1	B	F	F	29	25	**46**	91	1.4	**G**
503_3	F	F	G	34	44	**63**	85	2.2	**G**
504_1	B	F	G	61	24	**71**	83	4.5	**G**
506_1	F	G	G	83	31	**88**	85	2.8	**G**
506_3	F	G	G	56	43	**75**	93	2.2	**G**
506_4	F	B	F	6	17	**22**	85	3.6	**G**
511_1	F	F	G	62	39	**77**	90	2.2	**G**
511_2	F	G	G	46	28	**61**	92	2.2	**G**
511_3	F	G	G	89	35	**93**	83	4.1	**G**
512_1	F	F	F	25	21	**40**	81	3.0	**G**
512_3	G	F	G	35	42	**63**	82	3.6	**G**
519_1	F	B	F	60	0	**60**	51	15	**F** (1)
520_1	B	B	G	32	31	**53**	81	4.5	**G**
520_5	B	F	F	42	28	**58**	84	4.0	**G**
522_7	B	F	F	25	41	**55**	85	1.0	**G**
523_1	F	F	B	17	31	**43**	79	4.1	**F** (2)
523_3	G	F	B	24	9	**31**	88	1.0	**G**
536_3	F	F	G	56	39	**73**	91	2.2	**G**
541_1	G	G	G	90	41	**94**	93	2.2	**G**
541_3	G	G	G	90	38	**94**	92	2.0	**G**
546_1	F	F	G	87	39	**92**	84	2.2	**G**
549_1	G	F	F	37	37	**60**	71	1.4	**G**
552_1	F	F	F	66	0	**66**	54	15.3	**F** (1)
553_3	G	G	G	84	22	**88**	78	5.8	**G**
554_4	G	G	G	90	34	**93**	95	2.0	**G**
557_3	G	F	G	90	0	**90**	61	9.2	**F** (1)
558_1	G	G	G	90	5	**90**	52	15.3	**F** (3)
559_1	G	G	G	90	26	**93**	89	2.0	**G** (3)
559_3	G	G	G	90	16	**92**	80	4.2	**G**
561_1	B	F	B	15	42	**51**	63	11.2	**F** (3)
561_2	G	G	F	58	25	**68**	82	6.0	**G**
564_2	F	G	F	66	32	**77**	68	9.1	**G**

(1) OD hidden because of insufficient pupillary dilation
(2) OD has an irregular contour
(3) Slightly miscentered template

- the distance Δ between the centers of the regions T and D;
- a qualitative evaluation of the final ODDQ.

Table I provides details about these performance measures for each image in our database. One can see that our procedure correctly positioned the best template candidate within the true OD area on all the images of the database (0% false detection rate). Of course, the OD positionning is not always perfect but the global performace reaches our goal: the average OD area overlap and center position difference being $S = 80\%$ and $\Delta = 4.6$ pixels, respectively. A mean overlap of 80% is considered good when taking into account that the ground truth has been traced by hand and that the template matching is not fully elastic (only the template radius can be adjusted). A mean position error of 4.6 pixels corresponds to a relative error of 7% assuming a mean OD diameter of 65 pixels in our images.

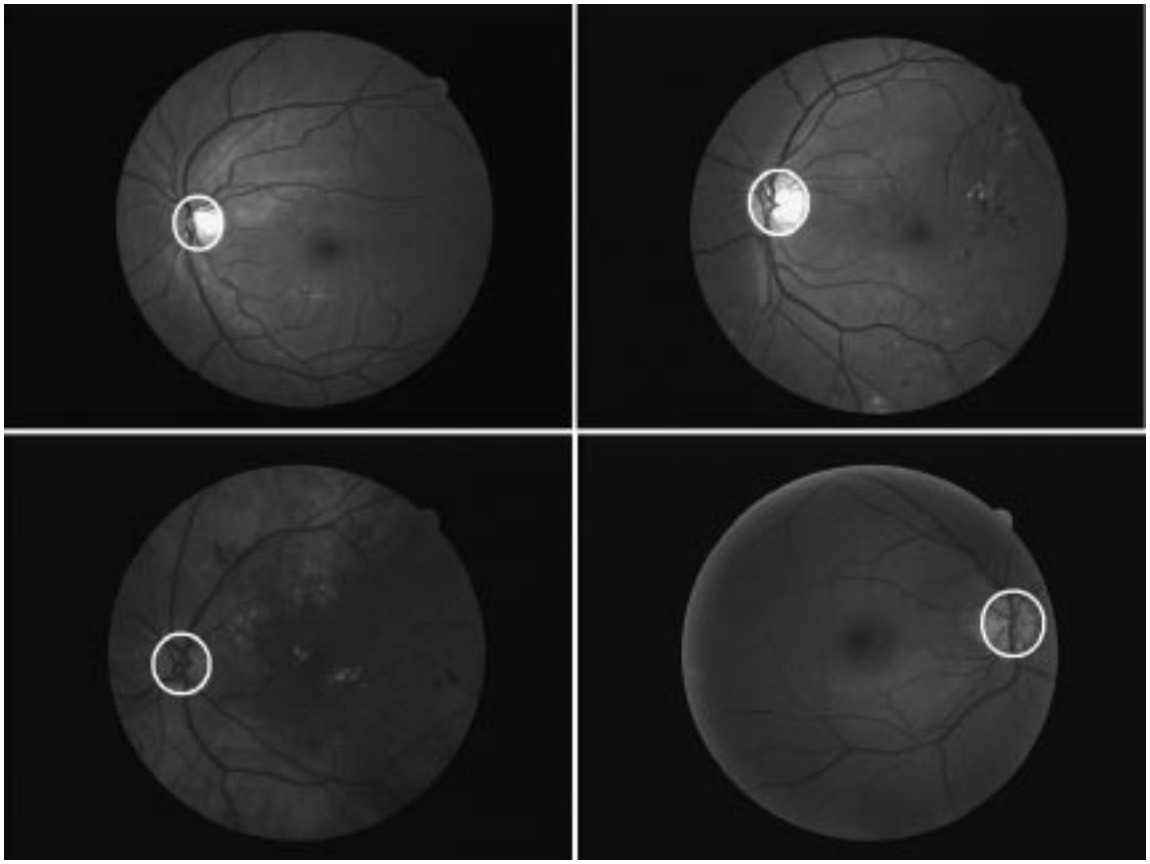

Fig. 4. Examples of OD detection on good-quality images. (top): 278_1 and 478_3; (bottom) 523_3 and 549_1. Only green band is displayed.

The ODDQ is the apparent quality of the detection result as evaluated by a human. ODDQ turns out to be good (G) for 34 images and fair (F) for the remaining six images (Table I). No detection can be qualified as bad. In all cases, the detector correctly pinpointed the OD region but slightly mis-centered the template for six of them.

Note that there is not necessarily a correlation between the ODDQ and the global confidence level C_G. In fact, C_G is more closely correlated with the IQ, ODCQ and ODBQ, meaning that a detection on a bad (good) quality image should be qualified by a low (high) confidence level regardless of the ODDQ. A low confidence value does not necessarily mean that the detection is apparently bad; it only provides an indicator for assessing the "level of difficulty" the detector had to identify the OD. This information is very useful in the context of computer-aided diagnosis as it can be combined with other informations to establish a general reliability index on a disease assessment, for instance.

The fact that C_G is always greater than $\max(C_H, C_R)$ results from two important hypotheses at the basis of the Dempster–Shafer theory: 1) evidence (or confidence) associated to a declaration is not a probability but rather a fuzzy variable and 2) evidence to a declaration *does not* imply complementary evidence to its negation (e.g., 60% of confidence that the detection is the correct OD does not imply that the remaining 40% is associated to non-OD detection). In Dempster–Shafer theory, the complementary evidence corresponds to the level of ignorance we have about a detection and part of this ignorance is responsible for increasing the global confidence C_G [12].

Figs 4 and 5 show examples of OD detections on representative images of the data set. The images show the green band on which the pyramidal and Hausdorff procedures are performed. Images in Fig. 4 are examples of good-quality images with good detections. Images in Fig. 5 are examples of fair- and bad-quality images with good or fair detections. A fair detection corresponds essentially to slightly mis-centered templates. These results are the most indicative of the robustness of the proposed approach.

C. Computational Performance

In addition to its robustness, another important advantage of the proposed approach is its fast computational time. In fact, the CPU time needed to process one image (640×480 pixels in size) on a Pentium III PC (700 MHz) running Solaris 7 is about 1 s for the pyramid stage and about 0.6 s (with a standard deviation of 0.3 s) for the Hausdorff stage. Computation time for the Hausdorff stage is dependent upon image content and it turns out to be smaller for lower values of P_{FA} because of the sparser edge map (pruning of the search space is more significant, hence the increase in processing speed).

IV. Discussion and Conclusion

We have reported about an OD segmentation algorithm in color fundus images which requires low computational search time, performs with a low false alarm rate and provides a confidence level on the detection that indicates the "level of difficulty" the detector has to identify the OD position and shape. The segmentation proceeds through the cooperation between (1) large scale object positioning using a multiresolution image decomposition and (2) template matching technique on edge maps using a Hausdorff distance measure. The use of complementary search techniques helps provide a reliable confidence level associated to the final detection result, which is a very useful information in the context of computer assisted diagnosis. Finally, one can mention the following observations/comments.

- The pyramid-based stage has a quite good success in pinpointing the OD region when the *a priori* knowledge about the OD position

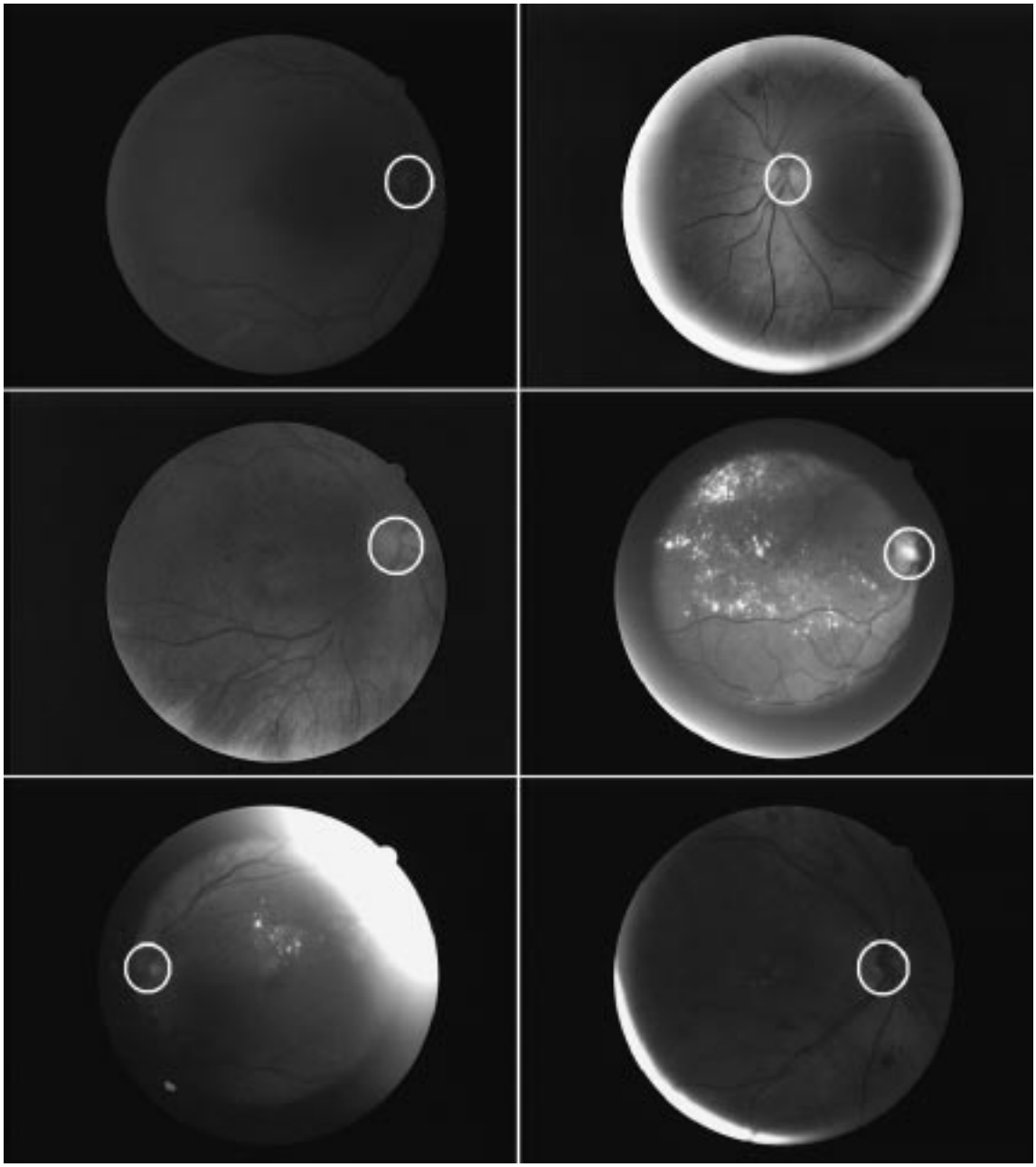

Fig. 5. Examples of OD detection on fair- and bad-quality images. (top) 501_1 and 501_4; (middle) 502_1 and 519_1; (bottom) 522_7 and 523_1.

is used. However, the position found is sometimes quite far from the true OD center and the pyramid approach is of no help in identifying the OD contour.

- The Hausdorff-based approach has very good success in finding the OD contour, thus the OD center, fast and reliably. However, it fails on images where OD contour is very diffuse.
- Each method compensates for a weakness of the other and combining both helps acieve a very satisfactory detection performance, even on poor quality images, along with a reliable detection confidence level. This is particularly important in the context of automatic image analysis for which a high confidence level solution is often a prerequisite for the reliability of additional image analysis stages.
- As one should expect, the performance of the approach proposed here is dependent upon the completeness of the thresholded edge map, meaning that thresholding must remove noisy edges and yet preserve the OD contour. One should be aware, however, that there is a direct link between the completeness of the edge map and the similarity of the noisy edge distribution with the Rayleigh model. Whenever an input image is of dubious quality, there is a substantial risk that its noisy edge distribution would be markedly different from the model, leading to an improper threshold selection and a severely broken thresholded edge map.

In situations where better accuracy would be needed for the OD contour, the proposed method could serve advantageously as an initialization stage for more refined techniques such as deformable templates or active contours (see [13] for instance). It is well known that a significant drawback of Lagrangian-formulated active contours (as opposed to level-set methods) is the penalty regarding the quality of the final contour and the algorithm convergence speed when the initial snake is far from the final state. The procedure presented here could serve as a preparation stage for those algorithms.

Although the focus of the paper is on optic disc detection, other applications that require the localization of a rigid shape may be solved efficiently by the proposed combination of techniques, namely a rough positioning of the object and a more refined Hausdorff-based search in a "probabilistically" thresholded edge map, with hypothesis management within the framework provided by the evidence theory. Tumor detection in X-rays or microcalcifications in mammograms might be some examples of other applications. We plan to evaluate different contexts in the near future and also to investigate possible generalizations of our approach for the detection of nonrigid shapes.

ACKNOWLEDGMENT

The authors would like to thank Dr. M.-C. Boucher of the Département d'ophtalmologie at Hôpital Maisonneuve-Rosemont of Montréal for providing the image dataset.

REFERENCES

[1] Y. A. Tolias and S. M. Panas, "An unsupervised fuzzy vessel tracking algorithm for retinal images," *Proc. 6th IEEE Int. Conf. Fuzzy Systems (FUZZ-IEEE'97)*, vol. 2, pp. 325–330.

[2] B. Kochner, D. Schuhmann, M. Michaelis, G. Mann, and K.-H. Englmeier, "Course tracking and contour extraction of retinal vessels from color fundus photographs: Most efficient use of steerable filters for model based image analysis," in *Proc. SPIE Medical Imaging 1998*, pp. 755–761.

[3] M. Lalonde, L. Gagnon, and M.-C. Boucher, "Non-recursive paired tracking for vessel extraction from retinal images," in *Proc. Conf. Vision Interface 2000*, May 2000, pp. 61–68.

[4] M. Beaulieu, "Algorithme de detection de la macula sur les images de la retine," Centre de recherche informatique de Montréal, Montréal, Canada, Tech. Rep. CRIM-00/07-05, July 2000. In French.

[5] L. Gagnon, "Rapport d'avancement patrimoine VAI," Centre de recherche informatique de Montréal, Montréal, Canada, Tech. Rep. CRIM-00/06-04, June 2000. In French.

[6] S. G. Mallat, "A theory for multiresolution signal decomposition: The wavelet representation," *IEEE Trans. Pattern Anal. Machine Intell.*, vol. 11, pp. 674–693, July 1989.

[7] E. Reiher, Y. Li, V. D. Donne, M. Lalonde, C. Hayne, and C. Zhu, "A system for efficient and robust map symbol recognition," in *Proc. Int. Conf. Pattern Recognition*, vol. 3, Aug. 1996, pp. 783–787.

[8] H. Voorhees and T. Poggio, "Detecting textons and texture boundaries in natural images," in *Proc. 1st Int. Conf. Computer Vision*, 1987, pp. 250–258.

[9] E. R. Hancock and J. Kittler, "Adaptive estimation of hysteresis thresholds," in *CVPR'91*, pp. 196–201.

[10] R. Ravid and N. Levanon, "Maximum-likelihood CFAR for Weibull background," in *Inst. Elect. Eng. Proc.-F*, vol. 139, 1991, pp. 256–264.

[11] D. P. Huttenlocher, G. A. Klanderman, and W. J. Rucklidge, "Comparing images using the Hausdorff distance," *IEEE Trans. Pattern Anal. Machine Intell.*, vol. 15, pp. 850–863, Sept. 1993.

[12] J. Hall, *Mathematical Techniques in Multisensor Data Fusion*. Norwood, MA: Artec House, 1992.

[13] F. Mendels, C. Heneghan, P. D. Harper, R. B. Reilly, and J.-Ph. Thiran, "Extraction of the optic disk boundary in digital fundus images," in *Proc. 1st Joint BMES/EMBS Conf.*, Oct. 1999, p. 1139.